Monthly Notices of the ROYAL ASTRONOMICAL SOCIETY

MNRAS **516,** 4932–4941 (2022) https://doi.org/10.1093/mnras/stac2587
Advance Access publication 2022 September 12

Two decades of X-ray observations of the isolated neutron star RX J1856.5 − 3754: detection of thermal and non-thermal hard X-rays and refined spin-down measurement

Davide De Grandis [1]★ Michela Rigoselli [1]★ Sandro Mereghetti [1] George Younes,[2] Pierre Pizzochero,[3,4] Roberto Taverna,[5] Andrea Tiengo [6,1,7] Roberto Turolla[5,8] and Silvia Zane[8]

[1]*INAF, Istituto di Astrofisica Spaziale e Fisica Cosmica Milano, via A. Corti 12, I-20133 Milano, Italy*
[2]*Department of Physics, The George Washington University, Washington, DC 20052, USA*
[3]*Dipartimento di Fisica, Università degli Studi di Milano, Via Celoria 16, I-20133, Milano, Italy*
[4]*Istituto Nazionale di Fisica Nucleare, sezione di Milano, Via Celoria 16, I-20133, Milano, Italy*
[5]*Dipartimento di Fisica e Astronomia, Università di Padova, Via F. Marzolo 8, I-35131 Padova, Italy*
[6]*Scuola Universitaria Superiore IUSS Pavia, Palazzo del Broletto, Piazza della Vittoria 15, I-27100, Pavia, Italy*
[7]*Istituto Nazionale di Fisica Nucleare, Sezione di Pavia, Via A. Bassi 6, I-27100, Pavia, Italy*
[8]*MSSL, University College London, Holmbury St. Mary, UK*

Accepted 2022 September 8. Received 2022 September 8; in original form 2022 August 5

ABSTRACT

The soft X-ray pulsar RX J1856.5 − 3754 is the brightest member of a small class of thermally emitting, radio-silent, isolated neutron stars. Its X-ray spectrum is almost indistinguishable from a blackbody with $kT^{\infty} \approx 60$ eV, but evidence of harder emission above ~ 1 keV has been recently found. We report on a spectral and timing analysis of RX J1856.5 − 3754 based on the large amount of data collected by *XMM-Newton* in 2002–2022, complemented by a dense monitoring campaign carried out by *NICER* in 2019. Through a phase-coherent timing analysis we obtained an improved value of the spin-down rate $\dot{\nu} = -6.042(4) \times 10^{-16}$ Hz s^{-1}, reducing by more than one order magnitude the uncertainty of the previous measurement, and yielding a characteristic spin-down field of 1.47×10^{13} G. We also detect two spectral components above ~ 1 keV: a blackbody-like one with $kT^{\infty} = 138 \pm 13$ eV and emitting radius 31^{+8}_{-16} m, and a power law with photon index $\Gamma = 1.4^{+0.5}_{-0.4}$. The power-law 2–8 keV flux, $(2.5^{+0.7}_{-0.6}) \times 10^{-15}$ erg cm^{-2} s^{-1}, corresponds to an efficiency of 10^{-3}, in line with that seen in other pulsars. We also reveal a small difference between the 0.1–0.3 keV and 0.3–1.2 keV pulse profiles, as well as some evidence for a modulation above 1.2 keV. These results show that, notwithstanding its simple spectrum, RX J1856.5 − 3754 still has a non-trivial thermal surface distribution and features non-thermal emission as seen in other pulsars with higher spin-down power.

Key words: stars: individual RX J0420.0 − 5022 – stars: individual RX J1856.5 − 3754 – stars: neutron – X-rays: stars.

1 INTRODUCTION

Among isolated Neutron Stars (NSs), the so-called X-ray Dim Isolated NSs (XDINSs) represent a peculiar class of nearby sources, characterized by their thermal emission in the X-ray band, with faint optical counterparts and no confirmed detection of radio signatures (e.g. van Kerkwijk & Kaplan 2007; Turolla 2009). Their very soft ($kT \lesssim 100$ eV) X-ray spectra are well reproduced by a simple blackbody with little interstellar absorption, with the additional presence of broad absorption lines in most sources (Haberl et al. 2003; Haberl et al. 2004; van Kerkwijk et al. 2004; Zane et al. 2005), and narrow, phase-variable ones in few cases (Borghese et al. 2015, 2017). These properties make XDINSs ideal study cases for models of NS thermal emission; this, in conjunction with their number, gained them the nickname of *Magnificent Seven*.

In particular, RX J1856.5 − 3754 (in the following J1856 for short, Walter, Wolk & Neuhäuser 1996) is the brightest ($f_X \simeq 1.5 \times 10{-}11$ erg cm^{-2} s^{-1}) and closest ($d = 123^{+11}_{-15}$ pc, Walter et al. 2010) of the group, as well as the one showing the scantest amount of timing and spectral features. Its pulsation – at $P = 7.05$ s (Tiengo & Mereghetti 2007) and $\dot{P} = 3 \times 10^{-14}$ s s^{-1} (van Kerkwijk & Kaplan 2008) – is hardly noticeable, due to a very small pulsed fraction PF $\simeq 1.2\%$. Its X-ray spectrum resembles, to an excellent degree of accuracy, a pure blackbody emission with temperature $kT^{\infty} \approx 60$ eV (Burwitz et al. 2001, 2003), even though the emission in the optical band requires the presence of a complex emission mechanism and/or thermal structure (Pavlov et al. 1996; Pons et al. 2002; Ho et al. 2007). In fact, J1856 has been detected at optical wavelengths, too ($V \sim 25.7$, Neuhaeuser et al. 1997). The optical spectrum follows a λ^{-4} law, but it lies above the extrapolation of a single-temperature X-ray blackbody at low energies.

The brightness, simple spectrum, and steadiness of its emission make J1856 an ideal target for the calibration of X-ray telescopes (Beuermann, Burwitz & Rauch 2006), and hence a very frequently observed object. In particular, *XMM-Newton* observed it about every six months, around April and October, since 2004 (with an earlier

★ E-mail: davide.degrandis@inaf.it (DDG); michela.rigoselli@inaf.it (MR)

single observation in spring 2002). This large amount of data allows detailed spectral and timing studies.

Using all the 2002–2011 data from the *XMM-Newton* EPIC-pn camera, Sartore et al. (2012) (in the following Sar+12) found that the X-ray spectrum of J1856 is indeed well described by a blackbody and set tight limits on possible spectral or flux variations. In addition, the high counting statistics allowed them to point out small instrumental systematic effects. In particular, the derived best fit blackbody temperatures depend slightly on the position of the source on the detector. More recently, Yoneyama et al. (2017) and Dessert, Foster & Safdi (2020) reported evidence for a flux enhancement above ≈1 keV with respect to the blackbody model. This excess indicates a spectral shape more complex than a single blackbody, possibly related to atmospheric effects and/or to the presence of a faint non-thermal emission component.

Here, thanks to the new wealth of data collected by *XMM-Newton* in the last decade, we extend the work by Sar+12 and revisit the spectral and timing properties of J1856, using also data from the Neutron Star Interior Composition Explorer (*NICER*) to derive an improved timing solution. The paper is organized as follows: in Section 2, we describe the data reduction; in Section 3, we present the spectral analysis, addressing in particular the systematics associated with the detector and the detection of a significant hard X-ray component; in Section 4, we present the coherent timing solution and pulse profiles resolved in different energy ranges; we discuss our findings in Section 5 and draw our conclusions in Section 6.

2 OBSERVATIONS AND DATA REDUCTION

This work is based on data collected between 2002 and 2022 by *XMM-Newton* and in 2019 by *NICER*. A log of all the observations is given in Tables B1 and B2.

For *XMM-Newton*, we used data collected by the EPIC-pn camera, reprocessed and analysed using the *XMM-Newton* Science Analysis System (SAS) version 20.0.0 and the latest calibration files. The observations were conducted with the EPIC-pn camera operated in Prime Small Window mode, yielding a time resolution of 5.7 ms. In order to exclude time intervals contaminated by a high background due to soft proton flares, for each observation we computed the distribution of high-energy count rates ($E > 10$ keV) binned at 100 s. The peaks of these distributions were then fitted with a Gaussian profile, and we discarded all the time intervals in which the count rate was more than $4\,\sigma$ apart from its mean. Thus, we obtained a net exposure time of 1.43 Ms of clean data.

For the spectral analysis we selected only EPIC-pn single-pixel events (PATTERN = 0). Most of the observations employed the thin optical filter; we discarded those taken with other filters, as well as the observation from 2011 October (# 17 in the log), as it was split over four short intervals in which the source was in a CCD position quite far apart from those of the other observations (see the discussion in Section 3.1). On the other hand, for the timing analysis, we used the whole set of observations and considered also double-pixel events (PATTERN ≤ 4) in order to maximise the counting statistics.

For the timing analysis, we also used a set of observations collected by *NICER*. We reduced the data with the NICERDAS software (version 9) including all the most recently released patches and calibration files (CALDB XTI20210720). We filtered the data using NICERL2 as part of heasoft version 6.30.1 and the standard cuts.

We converted the times of all the *NICER* and *XMM-Newton* events to the Solar system barycenter using the JPL ephemerides DE405 and the source nominal position R.A.=$18^{\rm h}\ 56^{\rm m}\ 35^{\rm s}.795$, Dec. = $-37^\circ 54' 35''.4$ (Walter et al. 2010).

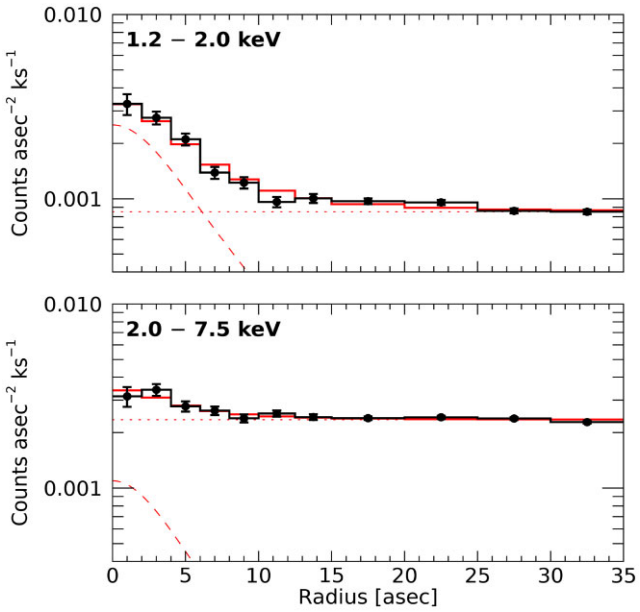

Figure 1. Surface brightness radial profiles of J1856 in the 1.2–2 keV (upper panel) and 2–7.5 keV (lower panel) energy bands. The red solid lines are the expected profiles, given by the sum of the instrument PSF (dashed) and a spatially uniform background (dotted).

3 SPECTRAL ANALYSIS

The X-ray emission from J1856 is extremely soft, with the great majority of the photons detected below ≈1 keV. The counting statistics in this range is so large that subtle instrumental effects and calibration uncertainties, which are generally neglected for fainter sources, are clearly visible (see Section 3.1).

On the other hand, the source is very faint at higher energies, where it can be detected only by summing many *XMM-Newton* observations. Therefore, for the analysis at energies above 1.2 keV, we used a maximum-likelihood (ML) method as described in Rigoselli et al. (2021, and references therein). For faint sources, this method is more effective than standard spectral analysis because it fully exploits all the counts distributed according to the instrumental point spread function (PSF), and it estimates the background locally, instead than from separate regions of the CCD. In the whole ML analysis, we used both single- and double-pixel events.

Based on the instrumental positions of the source in each observation, as measured in the 0.4–0.5 keV range where the signal to noise is highest, we realigned all the observations to correct for small pointing differences, and then stacked them to produce summed images in the 1.2–2 keV and 2–7.5 keV ranges. Applying the ML source detection to these images, we obtained 817 ± 57 and 327 ± 64 net source counts in the two energy ranges, corresponding to a detection significance of $18.2\,\sigma$ and $5.5\,\sigma$, respectively. Fig. 1 shows the radial profiles of J1856 between 1.2–2 keV (upper panel) and 2–7.5 keV (lower panel), compared to those expected for a point source in these energy ranges (red lines, see Ghizzardi 2002). In order to extract the spectra and pulse profiles at $E > 1.2$ keV described below, we applied the same ML methods to images accumulated in different energy and/or phase intervals.

3.1 Long-term behaviour in soft X-rays

We first investigated the possible long term evolution of J1856 by a spectral analysis of its 0.16–1.2 keV flux (the same energy range

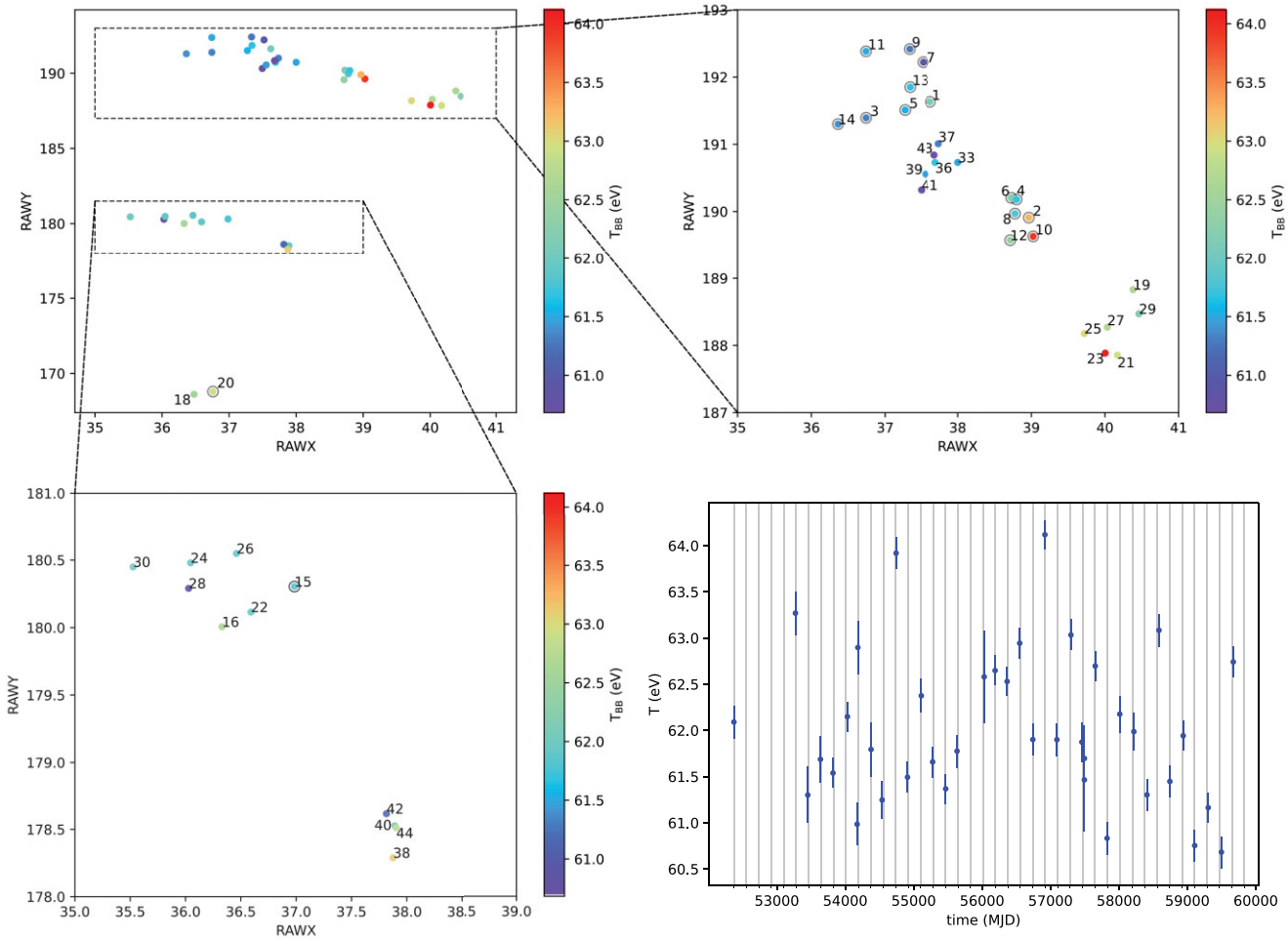

Figure 2. Top-left panel: Position of the source on the detector in raw coordinates (the top-right and bottom-left panels are zoomed views of the regions in the insets). The colours indicate the temperature obtained from the single blackbody fit and the labels correspond to the observation numbers of Table B1. The circled points are the observations already analysed by Sar+12; note, in particular, the two clusters they form in the top-right panel. Bottom-right panel: Temperatures obtained from the single blackbody fits as a function of time. The vertical lines are spaced by 6 months to highlight the seasonal cadence of the observations.

explored in Sar+12) in the individual *XMM-Newton* observations. The source counts were extracted from circular regions with 30 arcsec radius and the background counts from circles of radius 40 arcsec located as far from the source as possible, within the Small window field of view. The spectra were then rebinned to have at least 25 counts per bin.

We performed a simultaneous fit of the individual spectra with an absorbed blackbody model, letting the three fit parameters for each observation free: we found hydrogen column densities in the range $N_{\rm H} = [2 - 11] \times 10^{19}\,{\rm cm}^{-2}$, and observed temperatures in the range $kT^{\infty} = [60.7 - 64.1]\,{\rm eV}$($\chi^2 = 6421.00$ with 5421 dof); these values are shown in Fig. 2 as a function of time and position of the source on the detector. We repeated the fit with all the column densities linked to a common value, finding $N_{\rm H} = (3.95 \pm 0.08) \times 10^{19}\,{\rm cm}^{-2}$; the blackbody temperatures and normalizations show an analogous pattern and are within $2\,\sigma$ from the values of the previous fit ($\chi^2 = 6689.30$ with 5460 dof).

Even though the derived temperatures are in a narrow interval, they are not compatible with each other if only the statistical errors of the fits are considered. No discernible trend of temperature as a function of time and/or season of the observation is present. With a similar analysis of the data taken before 2010, Sar+12 noted that the temperature depends on the position of the source on the CCD (encoded by the RAWX and RAWY coordinates). We found similar results, but the new data acquired after 2011 indicate a more complicated pattern of position-dependent values than that shown by the older data. The lack of a clear pattern of this systematic effect makes it impossible to select a group of observations more reliable or well behaved than the others, as it was done by Sar+12. Although this prevents a precise estimate of the intrinsic thermal evolution of J1856, we are able to rule out a variation of more than few eV over the ≈ 20 yr time period we considered.

Given these instrumental effects affecting the derived parameters, in the following we will analyse the total spectrum (sum of all the spectra from the single observations) introducing a systematic error of 1% in the spectral fits. The best fit with an absorbed blackbody to the total spectrum, binned with a minimum of 200 counts per bin, is shown in Fig. 3; it gives $kT^{\infty} = 62.51 \pm 0.05\,{\rm eV}$ and normalization corresponding to an observed emission radius of $R^{\infty} = 4.74 \pm 0.02\,{\rm km}$ ($\chi^2 = 318.38$ with 169 dof). The fit residuals indicate the presence of a hardening above $\sim$1 keV, which was undetectable in the spectra of the single observations and will be investigated in the next subsection. Note that the residuals at $E < 0.6\,{\rm keV}$, highlighted in the figure inset, are at the level of only $\lesssim 2\%$,

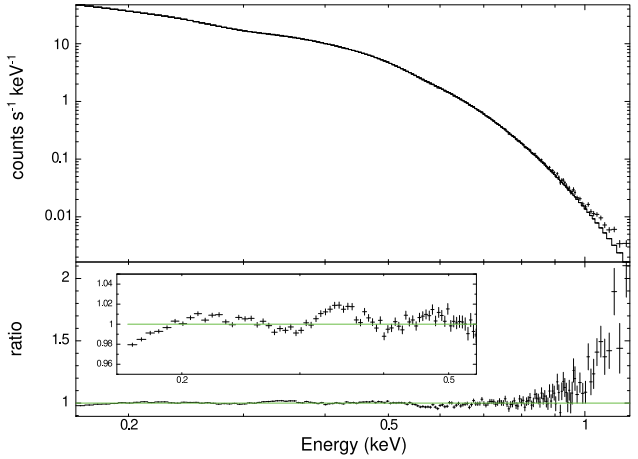

Figure 3. Total (summed) spectrum of all the data in the [0.16–1.2] keV band fitted with single blackbody. The bottom panel shows the ratio between the data and the folded model, highlighting the presence of a hard excess. The zoomed in version of the ratio below 0.6 keV in the inset shows that the residuals are at a level $\lesssim 2\%$, well below the instrument effective area uncertainties.

well below the current uncertainty of the instrument effective area calibration (e.g. Read, Guainazzi & Sembay 2014). Furthermore, the width of these deviations is narrower than the EPIC-pn energy resolution at these energies. Therefore, they do not imply the presence of spectral features in the X-ray emission of J1856.

3.2 X-ray spectrum

Given the statistically significant detection of J1856 also above 1.2 keV, we now consider the spectrum in the whole 0.2–7.5 keV range. In order to fit the excess with respect to the single blackbody, we first tested the addition of a second component, either a blackbody or a power law. Both models gave formally acceptable fits ($\chi^2 = 184.28$ and $\chi^2 = 167.89$ with 171 dof, respectively) because the χ^2 values are dominated by the good matching of the blackbody in the low energy range. However, the residuals indicate that these models are not a good description of the spectra above ∼1 keV (see the two bottom panels of Fig. 4).

An acceptable fit is obtained with a three-component model, namely the sum of two blackbodies and a power law ($\chi^2 = 156.10$ with 169 dof, see the best-fitting parameters in Table 1 and Fig. 4). As explained above, the wiggles in the residuals below ∼0.6 keV are of instrumental origin. Alongside a blackbody component akin to the one found so far ($kT_1^\infty = 61.9 \pm 0.1$ eV, $R_1^\infty = 4.92^{+0.04}_{-0.06}$ km) that describes the softest part of the spectrum, a second, hotter and from a smaller emission area ($kT_2^\infty = 138 \pm 13$ eV, $R_2^\infty = 31^{+8}_{-16}$ m) is found. This accounts for most of the emission observed around ≈1.5 keV. At even higher energies, the emission is dominated by a power law with photon index $\Gamma = 1.4^{+0.5}_{-0.4}$, and flux in the 2–8 keV band of $(2.5^{+0.7}_{-0.6}) \times 10^{-15}$ erg cm^{-2} s^{-1}. Conversely, a model with a single blackbody and two power laws ($\chi^2 = 144.89$ with 169 dof), yields an unphysically large photon index ($\Gamma \sim 6$) for the additional power-law component.

4 TIMING ANALYSIS

4.1 Coherent timing solution

We start our timing analysis of J1856 by utilizing the *NICER* observations, which were taken with heavy cadence and long exposure

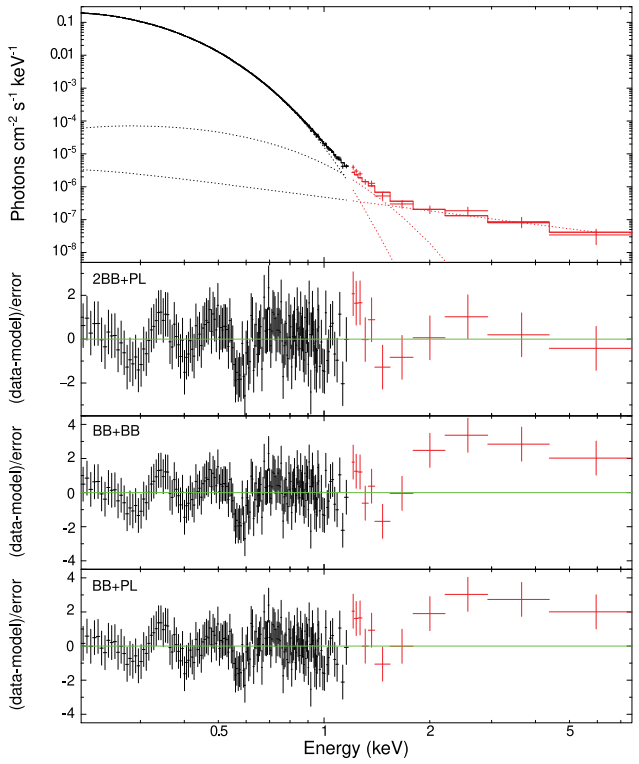

Figure 4. Top panel: Total X-ray spectrum obtained with the traditional background subtraction method (soft part, in black) and the ML method (hard part, in red). Out best-fitting model with two blackbody and a power-law components is superimposed in the top panel. The three bottom panels show the residuals for the two-blackbody plus power law fit (2BB+PL) itself, for the two blackbody (2BB) fit, and for the blackbody plus power law (BB+PL) fit (note the different vertical scale in the latter cases). We reject the two latter models which yield unsatisfactory residuals at $E > 1$ keV.

in the period from 2019 April 01 until 2019 April 07. During this time span and with an exposure totalling 60 ks, we collect ≈6×10^5 counts in the energy range 0.2–1 keV. We apply a Z_1^2 search, i.e. Rayleigh test (Buccheri et al. 1983), around the expected source spin frequency, 0.1417 ± 0.0001 Hz. We detect a strong signal at $\nu = 0.1417392(1)$ Hz at a confidence level > 99.99% at epoch $t_0 = 58576.5$ MJD (TDB).

We refine and update this initial measurement through a phase-coherent timing analysis technique (e.g. Dall'Osso et al. 2003). Using the high signal-to-noise pulse profile corresponding to the above frequency, we derive a model of the source pulse shape in the 0.2 to 1 keV band, consisting in the fundamental of a Fourier series. Then, we divided the unbinned data in chunks comprising 10^5 counts and collected in a time span not exceeding 7 d. This number of counts ensures the detection of the pulse at a ∼3 σ level. We fit each unbinned light curve with the pulse model with the maximum likelihood estimate method and only allowing for a phase shift $\Delta\phi$ (see Livingstone et al. 2009; Ray et al. 2011, for more details). Finally, we fit these phase shifts to a polynomial of the form $\delta\phi = (t - t_0)\nu + 1/2(t - t_0)^2\dot{\nu} + 1/6(t - t_0)^3\ddot{\nu} + \ldots$, truncated at the highest significant term according to an F-test.

Between 2019 February and June, we derive 19 pulse times of arrival (ToAs) utilizing the *NICER* data. We can describe these pulse ToAs with a simple correction to the source spin frequency. This resulted in $\nu = 0.141739071(4)$ Hz at the same t_0 given above. A frequency derivative in this time span is not statistically required, and we derive a 3 σ upper limit of $|\dot{\nu}| < 3.0 \times 10^{-15}$ Hz s^{-1}.

Table 1. Best fit of the X-ray spectrum.

Component	Quantity	Value
	$N_{\rm H}$ (10^{19}cm^{-2})	$3.9^{+0.3}_{-0.3}$
Soft BB	kT^{∞} (eV)	$61.9^{+0.1}_{-0.1}$
	R^{∞} (km)	$4.92^{+0.04}_{-0.06}$
Hard BB	kT^{∞} (eV)	138^{+13}_{-13}
	R^{∞} (m)	31^{+8}_{-16}
PL tail	Γ	$1.4^{+0.5}_{-0.4}$
	$I_{[2-8]}$ (10^{-15} erg cm^{-2} s^{-1})	$2.5^{+0.7}_{-0.6}$
	systematic	1%
	χ^2 / dof	156.10/169
	nhp	0.75

Note. Radii are computed taking $d = 123$ pc (Tetzlaff et al. 2011); $I_{[2-8]}$ indicates the flux in the 2–8 keV band.

Table 2. Parameters of the timing solution.

Quantity	Value
MJD t_0 (TDB)	58 576.5
MJD range	52 372 – 59 673
ν (Hz)	0.14173907778(8)
$\dot{\nu}$ (Hz s^{-1})	$-6.042(4) \times 10^{-16}$
χ^2/ dof	83.4 / 52
ToA rms (s)	0.381
P (s)	7.055217345(4)
$\dot{P}$ (s s^{-1})	$3.0075(20) \times 10^{-14}$
$\dot{E}$ (erg s^{-1})	3.38×10^{30}
$B_{\rm s}$ (G)	1.47×10^{13}
τ_c (yr)	3.72×10^{6}

The small uncertainty on the spin frequency of 4×10^{-9} Hz allows us to extend our phase-coherence up to ± 1 year around t_0 without the loss of cycle count, even when $\dot{\nu}$ is close to the $3\,\sigma$ upper-limit value. Hence, we derive the ToAs from the *XMM-Newton* data that are within this time span. We follow the same technique to compute the ToAs, yet, we used each full *XMM-Newton* observation to derive one ToA given the relatively short exposure of each of them, based on data in the 0.1–1 keV range. With a baseline of 700 d, we observe a clear curvature in the pulse ToAs which can be well described by introducing a second term to the timing model, $\dot{\nu} = -6.1(4) \times 10^{-16}$ Hz s^{-1}.

Following the above methodology, we iteratively added more ToAs while refining our timing solution, ensuring that no cycle ambiguity exists at each step. We find that our full baseline, spanning about 20 yr, can be well described by a timing model including only ν and $\dot{\nu}$. This model results in a χ^2 of 83.4 for 52 dof and a root mean square (rms) residual of 0.054 cycle. The full timing model is presented in Table 2, while the residuals of the pulse ToAs in seconds are shown in Fig. 5. We, moreover, find a hint for a second derivative of the frequency $\ddot{\nu} = -1.2(7) \times 10^{-26}$ Hz s^{-2}, but the improvement of the best fit ($\chi^2 = 80.3$ for 51 dof) is marginal (F-test probability of 0.167).

We checked that our results are not significantly affected by the proper motion of J1856 ($\mu_\alpha = +325.86 \pm 0.21$ and $\mu_\delta = -59.22 \pm 0.18$ mas yr^{-1}; Walter et al. 2010). In fact, by applying the barycentric corrections with the different source positions in each observations, the derived ToAs vary by less than 0.011 s, that is three times smaller than each ToA rms (≈0.381 s).

4.2 Energy-resolved pulse profiles

We used the timing solution derived above to fold the counts of all the *XMM-Newton* observations in order to obtain the pulse profile between 0.1–1.2 keV, shown in the upper panel of Fig. 6. Its pulsed fraction is PF $\equiv$ (CR$_{\rm max}$ − CR$_{\rm min}$)/(CR$_{\rm max}$ + CR$_{\rm min}$) = (1.13 ± 0.07)%, where CR is the background-subtracted count rate. A fit with a sinusoid plus a constant gives a $\chi^2 = 21.9$ (for 7 dof, nhp = 0.0026, red line in Fig. 6). The phase corresponding to the peak is $\phi_0 = 0.640 \pm 0.007$ (blue vertical line).

We repeated the analysis in the 0.1–0.3 keV and 0.3–1.2 keV energy ranges (second and third panel of Fig. 6). The softer profile has a smaller PF = (1.04 ± 0.09) per cent and is not consistent with a sinusoid ($\chi^2 = 20.6$ for 7 dof, nhp = 0.0044), as it is more skewed; its peak trails ϕ_0 of 0.035 ± 0.012 cycles. Contrariwise, the harder profile, with PF = (1.53 ± 0.12) per cent, is consistent with a sinusoid ($\chi^2 = 6.2$ for 7 dof, nhp = 0.52), and its peak leads ϕ_0 of 0.041 ± 0.011 cycles. The different behaviour of the two profiles can be seen in the fourth panel of Fig. 6, where we plot the hardness ratio HR = (CR$_{0.3-1.2}$ − CR$_{0.1-0.3}$)/(CR$_{0.3-1.2}$ + CR$_{0.1-0.3}$) as a function of the phase. The 0.1–0.3 keV range is rather narrow compared to the instrumental resolution $\Delta E \sim 100$ eV [full width at half maximum (FWHM)] at these energies, meaning that this hardness ratio does not reflect exactly the relative intensity of the flux in the two energy ranges. However, this systematic effect reduces the phase-modulation of the hardness ratio, compared to that obtained with a perfect instrument. We therefore conclude that there is evidence for a slight phase-dependent spectral variation of the soft component.

We extracted the pulse profiles in the 1.2–2 keV and 2–7 keV using the ML method to derive the net source counts from images accumulated in 6 and 4 phase bins, respectively (see the two lower panels of Fig. 6). The energy range 1.2–2 keV has PF = (29 ± 11)% and $\phi_0 = 0.39 \pm 0.16$. Fitting these profiles with a constant yields a $\chi^2 = 8.14$ for 5 dof and $\chi^2 = 5.64$ for 3 dof, respectively. Although these values are not large enough to claim a significant detection of pulsations, the shape of the profiles and their broad alignment with those seen at lower energies suggest that also the flux at these energies is modulated at the spin period.

5 DISCUSSION

Thanks to the combined use of *NICER* and *XMM-Newton* which provided, respectively, observations with frequent sampling and spanning a long time period, we could obtain a phase-coherent timing solution for RX J1856.5 − 3754 extending over 20 years. The only previous measurement of the spin-down rate of this XDINS had been reported by van Kerkwijk & Kaplan (2008). These authors used *XMM-Newton* and *Chandra* observations taken from 2000 to 2007 to set a $2\,\sigma$ upper limit of $|\dot{\nu}| < 1.3 \times 10^{-14}$ Hz s^{-1}, through a non-coherent timing analysis. The derivation of a univocal phase-coherent timing solution was hampered by the large separation between the observations, which led to some ambiguities in the count of the star rotation cycles. Nevertheless, van Kerkwijk & Kaplan (2008) could derive the most likely phase-coherent solution, yielding $\dot{\nu} = (-5.98 \pm 0.14) \times 10^{-16}$ Hz s^{-1}. The new data analysed here allowed us to derive, unambiguously and without loss of phase-coherence, a much more precise measurement of the spin-down rate, $\dot{\nu} = (-6.042 \pm 0.004) \times 10^{-16}$ Hz s^{-1}. This value confirms the results by van Kerkwijk & Kaplan (2008) and consolidates the estimates of rotational energy loss rate ($\dot{E} = 3.95 \times 10^{46}\,\dot{P}/P^3$ erg s^{-1} $= 3.38 \times 10^{30}$ erg s^{-1}) and dipolar magnetic field

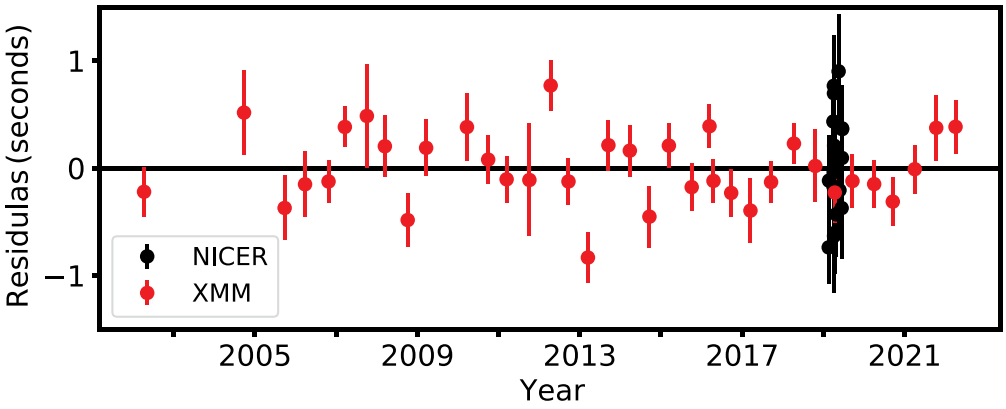

Figure 5. Residuals of the phase-connected timing solutions with $\nu = 0.14173907778(8)$ Hz and $\dot{\nu} = -6.042(4) \times 10^{-16}$ Hz s^{-1}.

($B = 3.20 \times 10^{19}\sqrt{P/\dot{P}}$ G $= 1.47 \times 10^{13}$ G). Moreover, we find that the spin-down has been remarkably stable over the two decades covered by our study (as proven by the very consistent spread of the residuals in Fig. 4 over time); this is in contrast to the other well studied XDINS RX J0720.4 − 23125, which shows long-term spectral and timing variability with a time-scale of a year (and references therein Hohle et al. 2012).

Our $\dot{\nu}$ measurement is consistent with the picture of J1856 as a typical member of the XDINS class. The characteristic age $\tau_c = P/2\dot{P} = 3.7$ Myr obtained from the dipole spin-down model is an order of magnitude higher than the kinematic age of 0.46 ± 0.05 Myr, obtained by tracing the proper motion of J1856 back to its likely birthplace in the Upper Scorpius association (Tetzlaff et al. 2011; Mignani et al. 2013). This is a manifestation of the dissipation and evolution of the magnetic field (e.g. Igoshev, Popov & Hollerbach 2021, and references therein), which is in line with the idea that XDINSs are older, worn-out magnetars.

Our spectral analysis confirms that J1856 is detected also above ≈1 keV and its spectrum is more complex than a single soft blackbody-like component. In fact, a hard excess has been detected up to ≈8 keV. It can be described with the sum of two components: a hot thermal one, dominating up to ≈2 keV, and a power law emerging at higher energy (see the results in Table 1). These two components had been separately detected in previous works: Yoneyama et al. (2017) found that the excess around ≈1 keV could be accounted for by a blackbody with $kT^{\infty} = 137^{+18}_{-14}$ eV, $R^{\infty} = 36^{+45}_{-36}$ m whereas Dessert et al. (2020) found a power law in the 2 and 8 keV band with $\Gamma = 1.0^{+1.1}_{-0.9}$, $I_{[2-8]} = (2.1 \pm 0.9) \times 10^{-15}$ erg cm^{-2} s^{-1}. We found that indeed both components are needed at the same time, and the parameter of our best fit are in good agreement with those reported by these authors.

The luminosity of the non-thermal component corresponds to 10^{-3} times the spin-down power $\dot{E}$. This value is consistent with what is observed in rotation powered X-ray pulsars with higher $\dot{E}$ (e.g. Possenti et al. 2002), so that a magnetospheric origin for this component appears as the most natural option. Nevertheless, the lack of a radio counterpart has recently led to more exotic suggestions, like the production of axion-like particles in the stellar core, to explain the hard power-law tail in J1856 (Buschmann et al. 2021). This may be tested for all the seven XDINS, and indeed Dessert et al. (2020) found evidence of a power-law tail in the spectrum of RX J0420.0 − 5022. We report in Appendix A our spectral analysis of this object. We find a hard excess with respect to a single component fit, which may be interpreted as a second blackbody in accordance with the results by Yoneyama et al. (2019), who found evidence of harder thermal components in all the XDINSs. However, the amount of data is not sufficient to constrain the nature of this hard excess, and in particular the presence of a non-thermal component at even higher energy cannot be unambiguously established. We nevertheless note that RX J0420.0 − 5022 and J1856 have the highest $\dot{E}$ of the class, so that they stand out as the most probable candidates to emit non-thermally. Further data will be needed to assess whether non-thermal emission is common to all the members of the XDINS class, or J1856 (and possibly RX J0420.0 − 5022) should be regarded as a separate NS flavour.

Of course, a significant detection of pulsations above ∼1.2 keV would give important clues on the origin of the hard X-rays. If the pulsations between 1.2–2 keV with a PF of about 30 per cent were confirmed, it would be natural to interpret the harder blackbody component as thermal emission from a hotspot on the star surface. The current data do not allow to draw firm conclusions, although the pulse profiles shown in Fig. 6 are intriguing. On the other hand, thanks to the large exposure time collected with *XMM-Newton* we discovered a statistically significant variation in the 0.1–0.3 keV to 0.3–1.2 keV hardness ratio, which indicates that the spectrum gets harder at the peak of the pulse profile. Furthermore, we found that the 0.1–0.3 keV pulse profile is somewhat skewed. These effects are noticeable below ≈1 keV, where the cooler blackbody dominates, and imply a certain degree of anisotropy in the thermal surface distribution and/or in the angular emission pattern. The dependence of the phase of the pulse maximum on the energy we found in J1856 bears some resemblance to what was reported in the magnetar XTE J1810 − 197 in outburst (Borghese et al. 2021) and may be again indicative of a non-axially symmetric thermal map.

Throughout this work, we described the thermal components of J1856 using blackbody models. This was not done merely for the sake of simplicity: we also tested models of emission from a magnetised atmosphere (namely, the NSMAXG models Ho, Potekhin & Chabrier 2008 for $B = 10^{13}$ G), finding that they consistently performed more poorly than the blackbody (χ^2/ dof $\gg 10$ in all instances). In fact, atmosphere models tend to produce a broader thermal spectrum throughout, rather than increasing the hard emission only. This points to the surface of J1856 being in some kind of condensed state, which shows an emission that is very close to a blackbody (van Adelsberg et al. 2005). Moreover, Rigoselli et al. (2022) showed that a relatively steep thermal map and atmospheric hardening produce a thermal spectrum that can be well fitted with two blackbody components, as long as $T_2/T_1 \sim 2$ and $R_2/R_1 \sim 0.1$. These values are suitable for the majority of the thermally emitting isolated NSs, with the exception of PSR J0633+1746 (Geminga), RX J0420.0 − 5022, and J1856 itself.

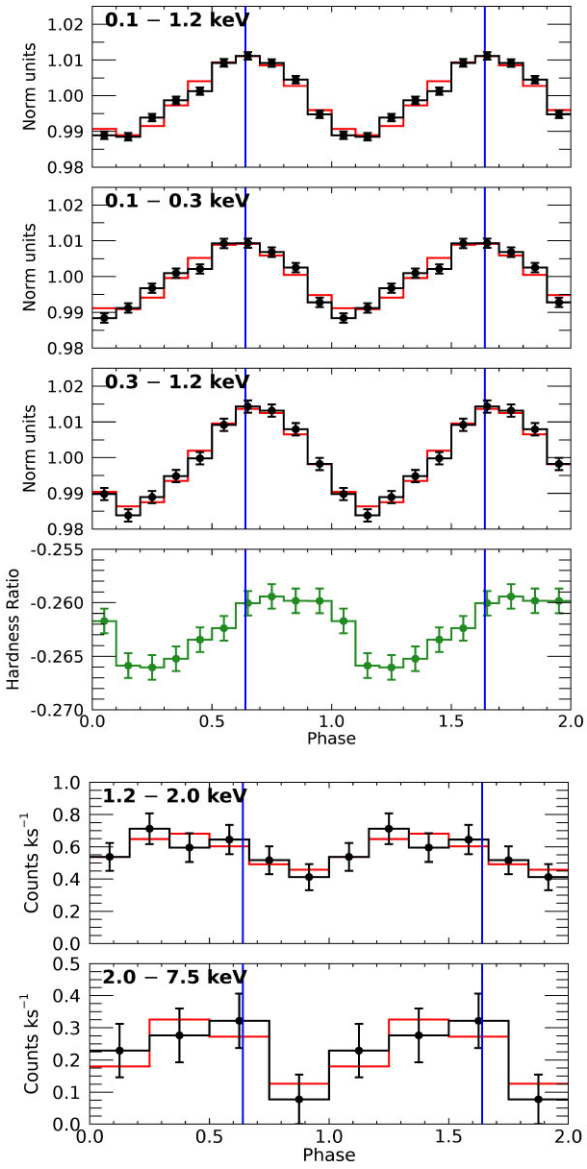

Figure 6. Pulse profiles between 0.1–1.2 keV (first panel), 0.1–0.3 keV (second panel), 0.3–1.2 keV (third panel), 1.2–2 keV (fifth panel), and 2–7.5 keV (sixth panel). The red lines show the best fit with a sinusoidal plus constant function, while the blue vertical lines show the phase corresponding to the peak ($\phi_0 = 0.640 \pm 0.007$). The fourth panel shows with green dots the hardness ratio between 0.1–0.3 keV and 0.3–1.2 keV as a function of the phase.

We finally note that the emission detected from J1856 in the optical band, consistent in with a Rayleigh tail (van Kerkwijk & Kulkarni 2001; Pons et al. 2002), requires the presence of a third, colder blackbody component. Indeed, our best fit model extrapolated to the optical/UV band still predicts a flux much lower than the observed one. At the same time, as found also in Sar+12, the inclusion of an additional blackbody component with $kT^{\infty} \simeq 30$ eV and emission area corresponding to the majority of the stellar surface ($R^{\infty} \simeq 16$ km) accounting for the optical flux, alters only marginally our best fit parameters of the X-ray components.

6 CONCLUSIONS

Our analysis of 1.43 Ms of data obtained with *XMM-Newton* over the last 20 yr showed that the X-ray spectrum of J1856 is more complex than originally believed and confirms independently reported evidence for emission above ∼1.2 keV. When coupled to the optical/UV observations, these data point to a neutron star shining mainly by thermal emission from a large fraction of its surface at an observed temperature of ∼62 eV. The remaining part of the star surface is a factor ∼2 cooler and is visible in the optical/UV band. We note that the ratios of these temperatures (∼2) and emitting radii (∼0.1) fit well with those of other thermally emitting NSs as shown in Fig. 7 of Rigoselli et al. (2022). The picture is complicated by the presence of a further hotter thermal component and a power-law tail. The former could result from a relatively small hotspot, consistent with the marginal evidence for pulsations in the 1.2–2 keV range, while the latter, if interpreted as non-thermal emission of magnetospheric origin, implies an efficiency in line with that observed for pulsars with higher $\dot{E}$. As the NS is isolated, the three thermal components are most likely an approximation of a more complex continuous thermal distribution on the surface resulting from its magnetothermal evolution; in particular, this points to a multipolar field structure (see e.g. the model proposed in De Grandis et al. 2021).

A phase-connected timing analysis shows a remarkable stability of the spin-down rate of J1856. Also its flux and spectrum remained virtually unchanged over a 20 years time span. Such properties were thought until recently to be shared by all the other XDINSs, with the notable exception of RX J0720.4 − 3125 (Hohle et al. 2012). However, new observations obtained with *eROSITA* (Mancini Pires, Schwope & Kurpas 2022) indicate the presence of long term variability in the spectral and timing properties of two more members of this class. These findings, together with the evidence that J1856 (and possibly RX J0420.0 − 5022) are not purely thermally emitting NS, indicate that, notwithstanding the small number of its representatives, the category of XDINSs is not so homogeneous. Future observations will have to appraise the merits and shortcomings of the XDINSs classification.

ACKNOWLEDGEMENTS

The results reported in this article are based on data obtained with *XMM-Newton*, an ESA science mission with instruments and contributions directly funded by ESA Member States and the USA (NASA) and by the NASA NICER mission and the Astrophysics Explorers Program. The data analysis has benefited from data and software provided by the High Energy Astrophysics Science Archive Research Center (HEASARC), a service of the Astrophysics Science Division at NASA/GSFC and the High Energy Astrophysics Division of the Smithsonian Astrophysical Observatory. We acknowledge financial support from the MIUR/PRIN grant UnIAM (2017LJ39LM, PI S. Mereghetti). GY research is supported by an appointment to the NASA Postdoctoral Program at the Goddard Space Flight Center, administered by Oak Ridge Associated Universities under contract with NASA.

DATA AVAILABILITY

All the data used in this article are available in public archives.

REFERENCES

Beuermann K., Burwitz V., Rauch T., 2006, A&A, 458, 541
Borghese A., Rea N., Coti Zelati F., Tiengo A., Turolla R., 2015, ApJ, 807, L20
Borghese A., Rea N., Coti Zelati F., Tiengo A., Turolla R., Zane S., 2017, MNRAS, 468, 2975

Borghese A. et al., 2021, MNRAS, 504, 5244
Buccheri R. et al., 1983, A&A, 128, 245
Burwitz V., Zavlin V. E., Neuhäuser R., Predehl P., Trümper J., Brinkman A. C., 2001, A&A, 379, L35
Burwitz V., Haberl F., Neuhäuser R., Predehl P., Trümper J., Zavlin V. E., 2003, A&A, 399, 1109
Buschmann M., Co R. T., Dessert C., Safdi B. R., 2021, Phys. Rev. Lett., 126, 021102
Dall'Osso S., Israel G. L., Stella L., Possenti A., Perozzi E., 2003, ApJ, 599, 485
De Grandis D., Taverna R., Turolla R., Gnarini A., Popov S. B., Zane S., Wood T. S., 2021, ApJ, 914, 118
Dessert C., Foster J. W., Safdi B. R., 2020, ApJ, 904, 42
Ghizzardi S., 2002, in Flight Calibration of the PSF for the PN Camera. XMM-SOC-CAL-TN-0029, http://www.cosmos.esa.int/web/xmm-newton/calibration-documentation
Haberl F., Schwope A. D., Hambaryan V., Hasinger G., Motch C., 2003, A&A, 403, L19
Haberl F. et al., 2004, A&A, 424, 635
Ho W. C. G., Kaplan D. L., Chang P., van Adelsberg M., Potekhin A. Y., 2007, MNRAS, 375, 821
Ho W. C. G., Potekhin A. Y., Chabrier G., 2008, ApJS, 178, 102
Hohle M. M., Haberl F., Vink J., de Vries C. P., Turolla R., Zane S., Méndez M., 2012, MNRAS, 423, 1194
Igoshev A. P., Popov S. B., Hollerbach R., 2021, Universe, 7, 351
Livingstone M. A., Ransom S. M., Camilo F., Kaspi V. M., Lyne A. G., Kramer M., Stairs I. H., 2009, ApJ, 706, 1163
Mancini Pires A., Schwope A., Kurpas J., 2022, preprint (arXiv:2202.06793)
Mignani R. P. et al., 2013, MNRAS, 429, 3517
Neuhaeuser R., Thomas H. C., Danner R., Peschke S., Walter F. M., 1997, A&A, 318, L43
Pavlov G. G., Zavlin V. E., Truemper J., Neuhaeuser R., 1996, ApJ, 472, L33
Pons J. A., Walter F. M., Lattimer J. M., Prakash M., Neuhäuser R., An P., 2002, ApJ, 564, 981
Posselt B., Popov S. B., Haberl F., Trümper J., Turolla R., Neuhäuser R., 2007, Ap&SS, 308, 171
Possenti A., Cerutti R., Colpi M., Mereghetti S., 2002, A&A, 387, 993
Ray P. S. et al., 2011, ApJS, 194, 17
Read A. M., Guainazzi M., Sembay S., 2014, A&A, 564, A75
Rigoselli M., Mereghetti S., Taverna R., Turolla R., De Grandis D., 2021, A&A, 646, A117
Rigoselli M., Mereghetti S., Anzuinelli S., Keith M., Taverna R., Turolla R., Zane S., 2022, MNRAS, 513, 3113
Sartore N., Tiengo A., Mereghetti S., De Luca A., Turolla R., Haberl F., 2012, A&A, 541, A66 (Sar+12)
Tetzlaff N., Eisenbeiss T., Neuhäuser R., Hohle M. M., 2011, MNRAS, 417, 617
Tiengo A., Mereghetti S., 2007, ApJ, 657, L101
Turolla R., 2009, in Becker W., eds, Neutron Stars and Pulsars, Astrophysics and Space Science Library, Volume 357. Springer Berlin Heidelberg, p. 141
van Adelsberg M., Lai D., Potekhin A. Y., Arras P., 2005, ApJ, 628, 902
van Kerkwijk M. H., Kaplan D. L., 2008, ApJ, 673, L163
van Kerkwijk M. H., Kaplan D. L., 2007, Ap&SS, 308, 191
van Kerkwijk M. H., Kulkarni S. R., 2001, A&A, 378, 986
van Kerkwijk M. H., Kaplan D. L., Durant M., Kulkarni S. R., Paerels F., 2004, ApJ, 608, 432
Walter F. M., Wolk S. J., Neuhäuser R., 1996, Nature, 379, 233
Walter F. M., Eisenbeiß T., Lattimer J. M., Kim B., Hambaryan V., Neuhäuser R., 2010, ApJ, 724, 669
Yoneyama T., Hayashida K., Nakajima H., Inoue S., Tsunemi H., 2017, PASJ, 69, 50
Yoneyama T., Hayashida K., Nakajima H., Matsumoto H., 2019, PASJ, 71, 17
Zane S., Cropper M., Turolla R., Zampieri L., Chieregato M., Drake J. J., Treves A., 2005, ApJ, 627, 397

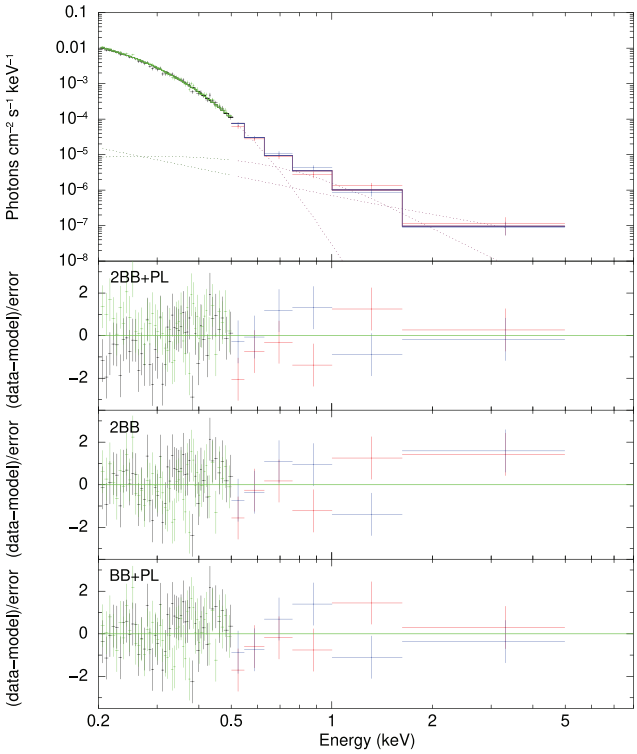

Figure A1. Same as Fig. 4 but for RX J0420.0 − 5022. The black/red points and curves correspond to the observations done in Small window mode, whereas the green/blue ones to the observations in Full frame.

APPENDIX A: SPECTRAL ANALYSIS OF THE XDINS RX J0420.0 − 5022

We analysed 19 EPIC-pn observations of RX J0420.0 − 5022, which span from 2002 to 2019 (see Table B3). We followed the same data reduction processes described in Section 2 and obtained 144 ks of net exposure time.

The source is well detected up to ≈0.5 keV, while at higher energies the spectrum is background-dominated. After checking that the bulk of the emission is constant throughout time, we stacked all the observations to produce summed images in the 0.5–1 keV and 1–5 keV ranges. Applying the ML source detection to these images in the two bands, we obtained 840 ± 38 (38.5 σ) and 173 ± 25 (8.7 σ) net source counts, respectively.

Then, we extracted the spectra taking care to group the observations according to the science mode in which the EPIC-pn was operating, in order to avoid cross-calibration uncertainties. The 5 observations taken in small window and the 14 observations taken in full frame provide similar exposure times: 68.5 ks and 75.8 ks, respectively. As we did for J1856, we extracted the soft spectrum (below 0.5 keV) with a standard analysis selecting only events with PATTERN = 0, whereas we extracted the hard spectrum (0.5–5 keV) with the ML technique (and PATTERN ≤ 4). The resulting spectrum is shown in Fig. A1.

We fitted simultaneously the four spectra (two for each science mode, divided over two energy ranges), finding that, in addition to the soft component fitted by a blackbody ($N_{\rm H} < 10^{19}$ cm^{-2}, $kT_1^{\infty} = 46.3^{+0.3}_{-0.5}$ eV, $R_1^{\infty} = 4.6^{+0.2}_{-0.1}$ km[1]) there is a hard excess that

[1]We used a distance of 335 pc, that is within the range 325–345 pc given by Posselt et al. (2007).

can be fitted either with a second blackbody ($kT_2^{\infty} = 210^{+30}_{-20}$ eV, $R_2^{\infty} = 17^{+3}_{-4}$ m, $\chi^2 = 94.36$ with 100 dof) or with a power law ($\Gamma = 3.10 \pm 0.25$, $I_{[2-8]} = (1.1^{+0.4}_{-0.3}) \times 10^{-15}$ erg cm^{-2} s^{-1}, $\chi^2 = 90.24$ with 100 dof). In both cases, there are no significant changes ($>2\,\sigma$) to the dominant blackbody component, nor to $N_{\rm H}$. This excess had already been described in Yoneyama et al. (2019) and our results are compatible with their findings.

We then tested a three component model, akin to the one used for J1856, but the improvement of the best fit is not significant: we obtained $\chi^2 = 89.51$ with 98 dof. When compared to the best fitting model of a blackbody plus a power law, this model yields an F-test probability of 0.67. The best-fit parameters, especially those of the power-law component, are poorly constrained: $kT_1^{\infty} = 46.1 \pm 0.6$ eV, $R_1^{\infty} = 4.6 \pm 0.2$; $kT_2^{\infty} = 170 \pm 50$ eV, $R_2^{\infty} = 22 \pm 6$ m; $\Gamma = 1.6^{+2.0}_{-0.6}$, $I_{[2-8]} = (2^{+18}_{-1}) \times 10^{-15}$ erg cm^{-2} s^{-1}. Therefore, we cannot confirm or dismiss the presence of two distinct hard components.

APPENDIX B: TABLES OF THE OBSERVATIONS

We report here the log of the observations used in this work: in Table B1 those from *XMM-Newton* and in Table B2 the ones from *NICER*. Table B3 reports the *XMM-Newton* observations of RX J0420.0 − 5022.

Table B1. The *XMM-Newton* observations used in this work. The filters are Thin1 (T1), Medium (M), and Thick (Tk), and for all the observations the EPIC-pn camera was operated in small window mode. The observations marked with a † were used only for the timing analysis and not for the spectral one.

#	Obs ID	Filter	Start date	Time (s)	Sar+12	#	Obs ID	Filter	Start date	Time (s)
1	106260101	T1	2002-04-08T16:22:29	58591	A	23	727760301	T1	2014-09-18T11:03:44	78912
2	165971601	T1	2004-09-24T01:42:13	33419	B	24	727760401	T1	2015-03-12T11:46:22	74514
3	165971901	T1	2005-03-23T08:34:42	35414	C	25	727760501	T1	2015-10-03T15:56:32	81916
4	165972001	T1	2005-09-24T07:58:13	35443	D	26	727760601	T1	2016-03-11T21:51:55	76917
5	165972101	T1	2006-03-26T15:40:29	70006	E	27	727761001	T1	2016-09-23T00:14:46	70916
6	412600101	T1	2006-10-24T00:31:14	73011	F	28	727761101	T1	2017-03-15T06:45:19	69817
7	412600201	T1	2007-03-14T20:50:01	69385	G	29	727761201	T1	2017-09-16T17:42:56	74512
8	412600301	T1	2007-10-04T05:48:55	70362	I	30	727761301	T1	2018-04-10T12:18:35	69064
9	412600401	T1	2008-03-13T18:47:14	74636	J	31†	791580101	Tk	2016-04-16T17:08:12	18416
10	412600601	T1	2008-10-05T01:00:58	68535	K	32†	791580201	M	2016-04-16T22:33:13	9810
11	412600701	T1	2009-03-19T21:30:04	68918	L	33	791580301	T1	2016-04-17T01:34:53	6419
12	412600801	T1	2009-10-07T12:06:44	81817	M	34†	791580401	Tk	2016-04-17T03:39:55	19317
13	412600901	T1	2010-03-22T02:48:57	73820	N	35†	791580501	M	2016-04-17T09:19:56	8914
14	412601101	T1	2010-09-28T23:09:10	69934	O	36	791580601	T1	2016-04-17T12:06:36	16418
15	412601301	T1	2011-03-14T00:45:15	83425	P	37	810840101	T1	2018-10-19T06:59:24	69516
16	412601401	T1	2012-04-13T07:14:06	77114	-	38	810840201	T1	2019-04-12T16:31:11	77889
17†	412601501	T1	2011-10-05T02:02:48	118098	Q	39	810841401	T1	2019-09-18T22:00:20	68915
18	412602201	T1	2013-03-14T08:26:38	73913	-	40	810841501	T1	2020-03-31T23:16:37	72918
19	412602301	T1	2012-09-20T11:25:04	80495	-	41	810841601	T1	2020-09-15T14:48:30	73520
20	415180101	T1	2007-03-25T05:36:47	40914	H	42	810841701	T1	2021-04-01T08:36:25	70416
21	727760101	T1	2013-09-14T14:20:54	71314	-	43	810841901	T1	2021-10-11T12:59:23	71911
22	727760201	T1	2014-03-26T06:00:22	73915	-	44	810842001	T1	2022-04-03T00:05:28	73914

Table B2. The *NICER* observations used in this work.

Obs ID	Start Date	Time (s)	Obs ID	Start Date	Time (s)	Obs ID	Start Date	Time (s)
1020520107	2019-02-16 03:02:37	3325	2614010109	2019-04-07 00:13:40	13177	2614010128	2019-05-22 16:20:37	1836
1020520108	2019-02-17 00:42:11	4096	2614010110	2019-04-08 02:11:20	2111	2614010129	2019-05-23 03:03:22	961
1020520109	2019-02-18 01:28:42	4195	2614010111	2019-04-08 23:43:46	5450	2614010130	2019-05-25 01:45:40	2566
1020520110	2019-02-19 00:41:08	7081	2614010112	2019-04-10 00:37:20	4409	2614010131	2019-05-26 01:01:00	865
1020520111	2019-02-20 01:28:20	649	2614010113	2019-04-11 02:50:00	5100	2614010132	2019-05-27 07:42:40	2931
1020520112	2019-02-21 06:52:00	1615	2614010114	2019-04-13 12:09:00	629	2012110103	2019-05-27 15:50:00	696
2020520102	2019-03-27 22:47:40	452	2614010115	2019-04-14 12:54:20	1668	2012120102	2019-05-27 17:23:00	338
2020520103	2019-03-28 00:31:10	7466	2614010116	2019-04-16 17:14:20	1204	2614010133	2019-05-28 00:44:00	190
2614010101	2019-03-30 20:42:19	735	2614010117	2019-04-19 10:08:00	1709	2012110104	2019-05-29 15:32:20	220
2614010102	2019-03-31 02:39:20	6027	2614010118	2019-04-21 02:26:24	2507	2614010134	2019-06-12 01:37:40	368
2614010103	2019-04-01 06:28:40	9325	2614010119	2019-04-22 00:15:40	8019	2614010135	2019-06-14 06:17:00	586
2614010104	2019-04-02 01:19:38	5758	2614010120	2019-04-27 02:40:00	2125	2614010136	2019-06-15 00:51:20	12915
2614010105	2019-04-03 01:32:18	5427	2614010121	2019-04-28 01:51:20	2594	2614010137	2019-06-16 04:43:00	1640
2614010106	2019-04-04 01:09:41	897	2614010122	2019-04-29 00:43:00	1365	2614010138	2019-06-17 03:20:45	13534
2614010107	2019-04-05 01:58:00	10883	2614010123	2019-05-05 11:01:21	95	2614010139	2019-06-18 01:10:40	5148
2614010108	2019-04-06 00:37:00	16429	2614010127	2019-05-17 19:13:40	51			

Table B3. The *XMM-Newton* observations of RX J0420.0 − 5022 used in this work. The science modes are Full frame (FF) and Small window (SW), and for all the observations the EPIC-pn camera was operated with thin optical filter.

Obs ID	Science mode	Start date	Time (s)	Obs ID	Science mode	Start date	Time (s)
141750101	FF	2002-12-30T03:38:44	17266	651470801	SW	2010-10-02T23:05:56	8086
141751001	FF	2002-12-31T21:54:49	9879	651470901	SW	2010-10-03T19:17:37	9034
141751101	FF	2003-01-19T16:42:18	14212	651471001	SW	2010-10-04T05:12:09	5285
141751201	FF	2003-07-25T21:21:51	17654	651471101	SW	2010-10-06T22:57:07	5611
651470201	SW	2010-03-30T11:55:07	2899	651471201	SW	2010-11-26T09:28:48	3748
651470301	SW	2010-04-04T18:56:28	2570	651471301	SW	2011-01-13T22:23:20	3866
651470401	SW	2010-04-09T08:34:36	5442	651471401	SW	2011-03-31T20:15:41	4783
651470501	SW	2010-05-21T05:50:13	2433	651471501	SW	2011-04-11T07:13:22	3622
651470601	SW	2010-07-29T14:20:46	4363	844140401	FF	2019-05-22T07:52:39	16753
651470701	SW	2010-09-21T08:40:34	6764				

This paper has been typeset from a TEX/LATEX file prepared by the author.